Aeroacoustics Conferences
20-23 May 2019, Delft, The Netherlands
25th AIAA/CEAS Aeroacoustics Conference

10.2514/6.2019-2633

Coherence Analysis of the Noise from a Simulated Highly-heated Laboratory-scale Jet

Kevin M. Leete* and Kent L. Gee †
Brigham Young University, Provo, Utah, 84602

Junhui Liu‡
Naval Research Laboratory, Washington, D.C. 20375

Alan T. Wall§
Air Force Research Laboratory, Wright-Patterson AFB, Ohio, 45433

Large-eddy simulations (LES) have been shown to reproduce the flow and acoustic fields of laboratory-scale jets with increasing accuracy. However, measurements of full-scale, high-performance military aircraft reveal phenomena that are not widely seen at laboratory scales. Recent modifications to LES methods allow for simulations of jets operating at a high temperature ratio, in a similar regime as military aircraft operating at afterburner. This work applies coherence analyses that have been previously used to study the jet noise field produced by military aircraft to the LES of a highly-heated, laboratory-scale jet. The coherence of the complex pressures along a near-field line approximately parallel to the shear layer shows evidence of four distinct field regions. The coherence between this line and complex pressures along the simulated jet lipline provide source regions in the jet plume corresponding to each field region. Differences in how information is transferred from the flow to the field suggests that the source regions represent different noise production mechanisms. The field regions compare favorably to some spatiospectral lobe features observed in measurements of an F-35B aircraft operating at afterburner, though do not reproduce all of the phenomena present in the aircraft's jet noise field.

I. Nomenclature

$\mathbf{A}$	=	Scaling matrix used to calculate $\mathbf{\Gamma^2(f)}$
BBSAN	=	Broadband shock-associated noise
$\mathbf{C}$	=	Cross-Spectral Matrix
D	=	Jet nozzle diameter
ETR	=	Engine thrust request
f	=	Frequency (Hz)
FWHS	=	Ffowcs Williams and Hawkings integration surface
G_{xx}	=	Autospectra of signal x
G_{xy}	=	Cross spectra between signals x and y
LES	=	Large eddy simulations
M_j	=	Jet Mach number
$\mathbf{p}$	=	Column vector that contains the complex pressures (Pa) for each measurement block for a single location
SPL	=	Sound Pressure Level (dB re 20 μPa)
U_j	=	Jet velocity (m/s)
x, y, z	=	Cartesian coordinates with origin at the nozzle exit (m)
$\mathbf{\Gamma}^2(f)$	=	Coherence matrix of an array for frequency f
$\gamma^2(f)$	=	Frequency-dependent coherence function
λ	=	Acoustic Wavelength (m)

*PhD candidate, Department of Physics and Astronomy, Brigham Young University, AIAA Student Member.
†Professor of Physics, Department of Physics and Astronomy, AIAA Member
‡Mechanical Engineer, Naval Research Laboratory, Washington, D.C. 20375, Senior AIAA Member
§Research Physicist, Battlespace Acoustics Branch, 2610 Seventh St., Bldg. 441, Wright-Patterson AFB, OH 45433, AIAA Member.

II. Introduction

The primary source of noise from high-performance military aircraft is the mixing of the jet exhaust with the ambient air. Due to the turbulent nature of the mixing, jet noise is not completely understood and remains a subject of study. Extensive measurements of the sound field, however, revealed that there are at least two field regions with different spectra and apparent source locations [1]. The field at large jet inlet angle (in the region of maximum radiation) has significant spatial coherence, a peaked spectrum, and an apparent source region downstream of the potential core. Towards the sideline, the spectrum is broader, has very low coherence, and an apparent source location throughout the mixing layer of the jet. These phenomena are consistent between laboratory-scale jets of many shapes, sizes, and speeds, allowing Tam *et al*. [2] to generate empirical similarity spectra to the shape of the spectra in the two regions. Before the late 1970s, turbulence in the jet plume was thought of as a large number of small turbulent eddies [3], though only the latter field type fit this idea. Visualization of larger structures in the flow [4, 5] led to the idea that the more coherent noise field downstream was due to radiation from large coherent structures.

Correlation analyses of laboratory-scale jets [6–8] between the measured flow and microphone recordings in the two acoustic field regions supported that the large-scale structures are responsible for the downstream coherent region and the small eddies throughout the mixing region were responsible for the sideline radiation. These general phenomena have come to be known as large-scale turbulence structures and fine-scale turbulent structures. Fine-scale turbulent structures are understood as small eddies or other perturbations in the mixing region of the flow, which exert an effective turbulence pressure on their surroundings [9], creating acoustic waves which propagate through the flow out to the ambient air. Due to counteracting effects of convection of the sound downstream by the flow and refraction as it transitions from the flow to the ambient air causes the sound to be nearly omnidirectional [10]. Large-scale turbulence structures have been thought to be due to Kelvin-Helmholtz instability waves generated in the shear layer of the jet at the nozzle [11], which grow as they convect downstream. The coherent nature of the instability waves causes directional radiation proportional to the supersonic speed at which the instabilities propagate downstream. If propagation is subsonic, the finite scale of the propagating disturbances causes portions of the wavenumber spectrum to be supersonic and generate acoustic waves efficiently.

This two-source model for jet noise is found to agree extremely well with laboratory-scale measurements of jets that operate at ambient to moderately hot temperatures. However, recent measurements of high-performance military aircraft, which operate at much higher temperatures than available at most laboratories, show deviations from the two-source model. Neilsen *et al*. [12] used measurements of a tied-down military aircraft operating at three engine conditions to show how the similarity spectra corresponding to the two-source model generally fit well, but with some notable exceptions. At higher engine conditions, the high-frequency slope of the measured spectrum was shallower than the large-scale turbulent structure similarity spectrum and the measured spectrum in the direction of maximum radiation exhibited two peaks. Neilsen *et al*. [13] also applied the same analysis to the jet noise field produced by an F-35, with similar results. Multiple peaks in the spectrum of high-performance military aircraft have been since reported on in several studies [12–23], with no conclusive explanation of their cause.

Leete *et al*. [15] used multisource statistically optimized near-field acoustical holography to investigate the field in the vicinity of a tied-down military aircraft operating at several engine conditions. They found that the region of maximum radiation is best represented by a superposition of several "spatiospectral" lobes. Spatiospectral lobes are local maxima in the space-frequency domain, where the spectra from multiple measurements across space are plotted side by side. Subsets of this phenomena are observed as a dual-peaked spectrum at a single microphone location in the field (such as observed by Ref. [12]) or a split directivity pattern in space at a single frequency. The relative amplitudes and spatiospectral slopes of the multiple lobes, which can vary greatly with engine condition, determine the directivity and peak frequency(ies) of the jet noise. These multiple spatiospectral lobes are observed in engine powers as low as 50% engine thrust request (ETR), which have temperatures closer to those achievable at the laboratory scale.

There have been limited reported observations of what could be considered spatiospectral lobes in laboratory-scale jets. One example is seen in the right pane of Fig. 7 of Ref. [24], where a spatiospectral map of the sound pressure levels measured at a dense array parallel to the jet centerline show maxima and minima. It is unknown if the phenomenon has gone largely unreported is because laboratory-scale jets do not operate at the conditions required to produce the lobes (high temperature, Mach number, etc.) or because many experiments do not sufficiently resolve the spatiospectral domain to observe it. Because high-fidelity LES simulations afford the opportunity to produce a finely-sampled spatiospectral domain in the radiated noise, analysis of LES data can provide important insights into phenomenological similarities between the flow from simplified jet nozzles and full-scale military jet engines.

Liu *et al*. [25–27] have adapted the Naval Research Laboratory's Jet Noise Reduction, JENRE, finite-element LES

solver to simulate temperatures similar to conditions of high-performance military aircraft. Spatiospectral domain analysis of the aft radiation shows a smooth transition from high-frequency components peaking with a directivity at at jet inlet angle of about 115°, to lower frequency content with a farther aft directivity of about 140° [26]. Based on instantaneous pressure maps of the field, they identify the higher-frequency, upstream content as Mach wave radiation due to its plane wave like unidirectional behavior. The lower frequency content which radiates at larger aft angles has a more stochastic radiation pattern with a less defined directivity. This is described as large-scale turbulent structure noise. The spatiospectral maps in Leete *et al*. [15] of the F-35B at afterburning engine powers between 0-700 Hz are qualitatively similar to Liu *et al*. [26] between 0-7000 Hz with one important distinction — the LES-generated spectra contain a smooth transition from the 155° peak to the 140° peak, whereas the F-35B contains upwards of five discrete spatiospectral lobes, which can cause a split directivity pattern in the field or a dual peak in the spectrum.

The primary goal of this paper is to gain physical insight into the jet noise field produced by the simulated high-temperature jet by applying analysis methods previously used to characterize the noise fields of high-performance military aircraft [15, 21, 28, 29]. Of particular interest is the separation of the field into different regions, characterization of their properties, and identification of probable source mechanisms within the flow for each region. Comparisons with previous analysis of the F-35 can then be made, where information about the flow is unknown.

III. LES of the highly-heated laboratory-scale jet

The LES data set in this work is provided by Liu *et al*. [25–27]. It uses the JENRE LES solver to predict the pressure and velocity fluctuations due to heated flow passing through a convergent/divergent nozzle and interacting with the ambient air. The JENRE solver uses a monotonically-integrated LES approach with a flux-corrected transport algorithm and explicit Taylor-Galerkin scheme. A temperature-dependent specific heat ratio has also been incorporated. The nozzle geometry and a representative pressure field can be seen in Fig 1 a) of Ref. [26]. The test conditions used in this study is a jet velocity of $U_j = 1175$ m/s (corresponding to a Mach number, M, of 3.38) resulting in an underexpanded, shock-containing jet. The ratio of the temperature of the flow to the ambient condition (TTR) is 7, which was chosen to be in the same regime as high-performance military aircraft operating at afterburner [30]. LES is used to compute the thermodynamic quantities in the flow region of the jet out to a conical surface outside of the main flow, and the pressures outside the surface were predicted using the Ffowcs Williams and Hawkings integration method. Time records of the LES simulation were split into 97 blocks and a Fourier transform applied to each block to give a complex pressure spectrum with a frequency spacing of about 150 Hz. Since the accuracy of the coherence calculations is dependant on the number of simulated measurement blocks and the frequency spacing in the spectra is dependant on the length of each block, it was necessary to run this simulation for much longer than generally is sufficient for time-domain analyses of LES. The total temporal duration of the simulation was 0.326 s, which covers 5260 D/U_J.

Figure 1 includes a schematic of the simulation with the nozzle exit, the Ffowcs Williams-Hawkings integration surface (FWHS), and two simulated arrays where the field was sampled. All lengths are nondimensionalized by the exit diameter, D, with the flow in the positive x direction and the origin at the center of the nozzle exit. The flow field was sampled along the nozzle lipline of the jet from the nozzle exit to $x/D = 25$. The acoustic field was sampled along the line $y/D = \frac{1}{6}x/D + 10$, from $x/D = -10$ to $x/D = 40$. The right panel of Fig. 1 shows the local Mach number of the fluid along the jet centerline (blue) and the ratio of the fluid velocity, U, to the jet velocity, U_j. The end of the potential core is estimated as $x/D = 7.2$, where $U/U_j \approx 0.95$ (red dashed line) and is marked with a red diamond. The end of the supersonic core is located at $x/D = 12.67$, where $M = 1$ and is marked with a blue diamond.

The normalized sound pressure levels along the field array are pictured in the left pane of Fig. 2. The spectra from each simulated array point between 0 and 7 kHz is shown. On the left, upstream of the nozzle exit, broadband shock-associated noise (BBSAN) is seen starting at about 3.5 kHz and shifting up in frequency to 7 kHz at about $x/D = 5$. Overall levels are the highest between 5 D and 30 D where the directional portion of the turbulent mixing noise is present. The peak frequency of the spectrum decreases as the array extends downstream.

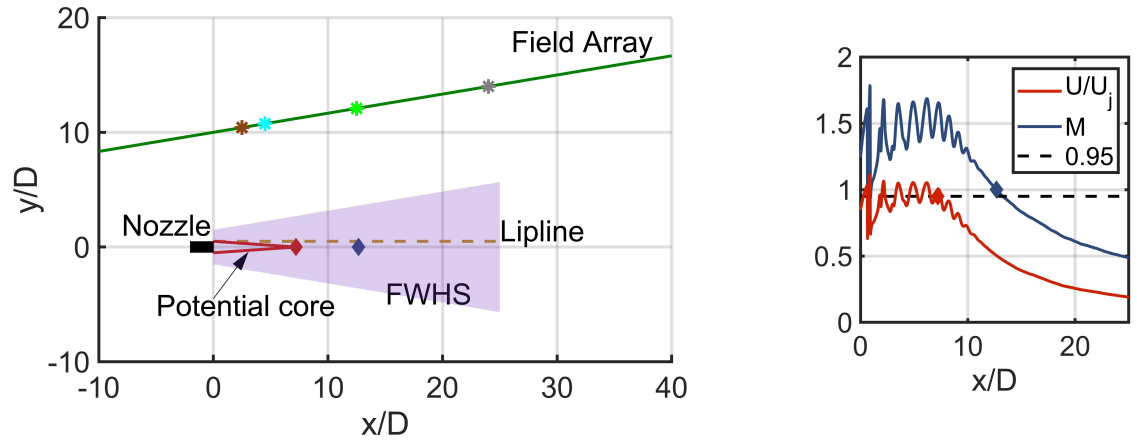

Fig. 1 Left: Schematic of the nozzle exit location, the two simulated measurement arrays used in this paper, the FWHS, and the approximate location of the potential core. Right: The Mach number and jet velocity ratio along the jet centerline. The red and blue diamonds show the locations of the end of the potential and supersonic cores respectively.

IV. Coherence Analysis

A. Coherence function

The frequency-dependent coherence function, $\gamma^2(f)$, is a frequency-domain analog of the correlation function, and is defined as

$$\gamma^2(f) = \frac{|G_{xy}(f)|^2}{G_{xx}(f)G_{yy}(f)}, \tag{1}$$

where G_{xx} and G_{yy} are the autospectra of arbitrary signals x and y and G_{xy} is their cross spectrum. The coherence is restricted to range $0 \leq \gamma^2 \leq 1$, where a value of one signifies that all of the time-averaged energy in y is linearly related to the energy in x at that frequency, and a value of zero means there is no relation. At two measurement points x and y, the complex pressures are arranged into $m \times 1$ (m is the number of blocks) column vectors $\mathbf{p}_x$ and $\mathbf{p}_y$. The coherence at a given frequency, f, between the points is then calculated by

$$\gamma^2(f) = \frac{|\mathbf{p}_x^{\mathrm{H}}\mathbf{p}_y|^2}{\mathbf{p}_x^{\mathrm{H}}\mathbf{p}_x\mathbf{p}_y^{\mathrm{H}}\mathbf{p}_y}, \tag{2}$$

where superscript H is the Hermitian transpose. This can be extended to generate a matrix $\mathbf{\Gamma}^2(f)$ whose entries are the $\gamma^2(f)$ between all combinations of points on two measurement arrays x and y with n_x and n_y elements each. This is done by defining

$$\mathbf{C} = \begin{bmatrix} \mathbf{p}_{x_1}^{\mathrm{H}} \\ \mathbf{p}_{x_2}^{\mathrm{H}} \\ \vdots \\ \mathbf{p}_{x_{n_x}}^{\mathrm{H}} \end{bmatrix} \begin{bmatrix} \mathbf{p}_{y_1} & \mathbf{p}_{y_2} & \cdots & \mathbf{p}_{y_{n_y}} \end{bmatrix} \tag{3}$$

and

$$\mathbf{A} = \begin{bmatrix} \mathbf{p}_{x_1}^{\mathrm{H}}\mathbf{p}_{x_1} \\ \mathbf{p}_{x_2}^{\mathrm{H}}\mathbf{p}_{x_2} \\ \vdots \\ \mathbf{p}_{x_{n_x}}^{\mathrm{H}}\mathbf{p}_{x_{n_x}} \end{bmatrix} \begin{bmatrix} \mathbf{p}_{y_1}\mathbf{p}_{y_1}^{\mathrm{H}} & \mathbf{p}_{y_2}\mathbf{p}_{y_2}^{\mathrm{H}} & \cdots & \mathbf{p}_{y_{n_y}}\mathbf{p}_{y_{n_y}}^{\mathrm{H}}, \end{bmatrix}. \tag{4}$$

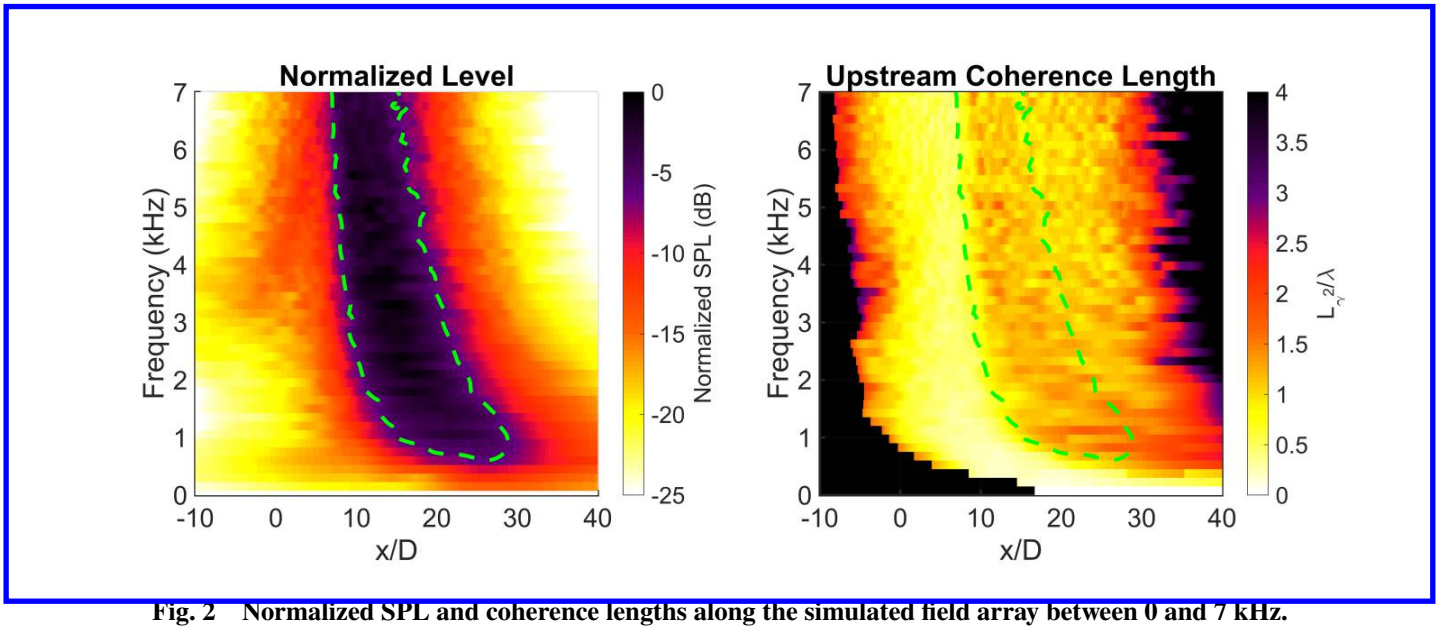

Fig. 2 Normalized SPL and coherence lengths along the simulated field array between 0 and 7 kHz.

The $n_x \times n_y$ coherence matrix $\mathbf{\Gamma}^2(f)$ can then be expressed as

$$\mathbf{\Gamma}^2(f) = \frac{|\mathbf{C}|^2}{\mathbf{A}}, \tag{5}$$

where $|\mathbf{C}|^2$ represents the magnitude squared of each element of $\mathbf{C}$ and the division of $\mathbf{C}$ and $\mathbf{A}$ is element-wise.

The i^{th} row of $\mathbf{\Gamma}^2(f)$ (Equation 5) is the coherence between the element x_i and all of the y_j's, and the reverse is true for the columns. If $\mathbf{\Gamma}^2(f)$ is calculated between an array and itself it is symmetric, square, and the diagonal elements are unity.

In Bendat and Piersol [31], equation 9.82 gives the normalized random error of the coherence calculation that depends on the calculated coherence and the number of complex pressure blocks used. For the number of blocks used in this study, a coherence estimation of less than 0.02 results in a normalized random error greater than one, meaning the true coherence could be in fact, zero. This gives a practical lower limit to the possible values of γ^2 obtainable in this study.

B. Field Coherence

The coherence matrix of a measurement array in the vicinity of a jet gives insight into the jet noise field properties. Prior studies have investigated the coherence properties of the F-35B [18] and correlative properties of an LES data set similar to the current one [32]. Since $\mathbf{\Gamma}^2(f)$ is a large matrix for each frequency, it is difficult to concisely visualize trends across frequencies. Recently, the coherence length [18, 28, 29, 33] has been shown to be a figure of merit in acoustical analysis of military jet noise. The coherence length, L_{γ^2}, is defined as the distance between two points along a measurement array where the coherence drops from unity to 0.5. If L_{γ^2} is calculated in a single direction, it allows for a single value to be calculated for each frequency and array position, which can then be displayed in a single plot. Figure 2 shows the normalized sound pressure levels along the field array (the green line in Fig. 1) and the corresponding upstream ($-x$ direction) L_{γ^2}. The coherence lengths are nondimensionalized by dividing by the acoustic wavelength (λ), as done in Ref. [18]. The plot is saturated to black at 4λ or when there were not enough upstream microphones in the array to mark a drop in coherence to 0.5. The green dashed line marks the level contour 6 dB down from the maximum and is repeated on the plot of the upstream coherence lengths for reference. This spatiospectral region is referred to as the region of maximum radiation in this work.

In Fig. 2, the largest values of L_{γ^2}/λ are found aft of $x/D = 30$, which appears to be due to the array being large compared to the aeroacoustic source. If the field is impinging on the array at grazing incidence, then the coherence along subsequent points in the array will be large, as little information is changed between points. Upstream of $x/D = 0$, L_{γ^2} is large in the 3-5 kHz band where the BBSAN signature is seen and increases towards the edge of the array. Coherence lengths are the lowest at about $x/D = 10$, where the radiation towards the sideline is broadband. In the maximum

radiation region coherence lengths generally stay between 1-2 wavelengths. At 0.5-1.5 kHz, there is a general increase in L_{γ^2}/λ downstream of 20 D which continues to the end of the array. As frequency drops to zero and wavelengths become very large compared to the dimensions of the jet flow, normalized coherence lengths naturally drop to zero.

Though L_{γ^2} serves as a useful glance at the entire field in one plot, the full story of the field can only be told by analysis of $\mathbf{\Gamma}^2(f)$. A single column of $\mathbf{\Gamma}^2(f)$ can be extracted for each frequency and compiled to create a coherence spectra of the array to the reference point corresponding to the chosen column. Parts a)-d) of Fig. 3 display the coherence spectrum of the array with respect to four reference points located at x/D = 2.5, 4.5, 12.5, and 24 respectively. These points were chosen to represent phenomenological trends observed as the coherence was examined for all points along the array. The vertical dashed lines represent the location of the reference, and their color matches the four indicators marked on the field array in Fig. 1. The coherence spectrum in Fig. 3 a) uses a reference chosen where the BBSAN signature is observed in Fig. 2. Faint traces of coherence can be seen between the reference point and 10 D downstream between 4 and 6 kHz. This faint trace of coherence is in the frequency range where the BBSAN level is the largest at the reference. Figure 3 b) shows the coherence spectrum with a reference point chosen where the coherence lengths in Fig. 2 were the lowest, just upstream of the region of maximum radiation. The coherence is small across all but the lowest frequencies.

Figure 3 c) shows the coherence of the array with a reference located in the maximum radiation region. The coherence is generally larger than seen in parts a) and b) as well as over a larger spatial extent, as is seen by the increase in L_γ^2/λ in Fig. 2. What is unseen in Fig. 2 is that in the region of maximum radiation, a single point in space contains frequency information that is coherent with the upstream BBSAN signature. Coherence between the BBSAN and the region of maximum radiation implies that either the BBSAN source is propagating downstream into the region of maximum radiation as well as upstream, or the source mechanisms (BBSAN source and the source contributing the region of maximum radiation) are not independent. If, for example, the BBSAN is caused by the actuation of the shock cells by instability waves convecting downstream, it stands to reason that the instability waves would transfer, at least partially, the shock fluctuation information to the acoustic field via their Mach wave radiation. The coherence alone cannot conclusively distinguish between these two possible explanations. Swift *et al*. [18] shows a similar pattern with their coherence analysis of the F-35.

Part d) of Fig. 3 shows that as the reference point is moved farther downstream, the coherence of the field increases with a larger increase in the 0.5 to 1.5 kHz range. Even though the reference is not completely removed from the region of maximum radiation, any evidence of coherence with the BBSAN disappears. It is possible this is caused by some change in the source mechanism responsible for the radiation to the field in that direction. There is some common coherence between parts c) and d) below 1 kHz. The coherence for frequencies above 1 kHz begin to saturate downstream of 25 D.

These observations of the field coherence allows for the separation of the field into four regions:

1) Region where the BBSAN signature dominates. The frequency-dependant signature peaks at a lower frequency upstream and shifts to higher frequency towards the sideline. Underneath the BBSAN there is uncorrelated noise present, so the coherence drops outside of the frequency band where the BBSAN peaks.
2) Region of low coherence, upstream of the contribution of the aft radiation and downstream of the BBSAN component.
3) The portion of the region of maximum radiation that shows traces of coherence with the BBSAN in region 1).
4) The portion of the region of maximum radiation where the coherence with region 1) disappears until the end of the array.

Regions 3), and 4) are similar to the two spatiospectral lobes identified in Ref. [26]. In an analysis of a cross-section of the instantaneous pressure field, qualitatively differing radiative properties are seen between the upstream and downstream portion of the region of maximum radiation. They attribute the upstream portion of the maximum radiation region (identified here as region 3)) to Mach wave radiation, because of the highly directional, plane-like propagation of the waves. The downstream, lower frequency portion (identified here as region 4)) is attributed to what they call "large-scale turbulent structure noise", where the radiation from the downstream portion of the flow is less well-ordered.

C. Flow Coherence

The advantage of investigating the field of this LES as opposed to measurements taken of full-scale aircraft is that flow velocities and pressures are known. Thus, the same coherence analysis that was done on the field can be repeated for the pressures along the nozzle lipline. Figure 4 shows the normalized sound pressure levels (left) as well as the normalized upstream coherence lengths (right) along the nozzle lipline. The wavelength used for normalization is the

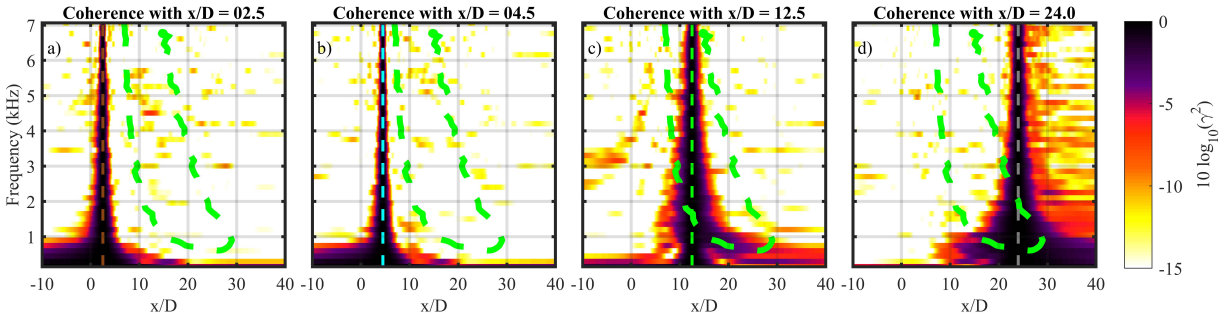

Fig. 3 Coherence of the field array with four different reference points along it: x/D = 2.5, 4.5, 12.5, and 24. The colored dashed lines representing the reference locations correspond to the colored marks on Fig. 1.

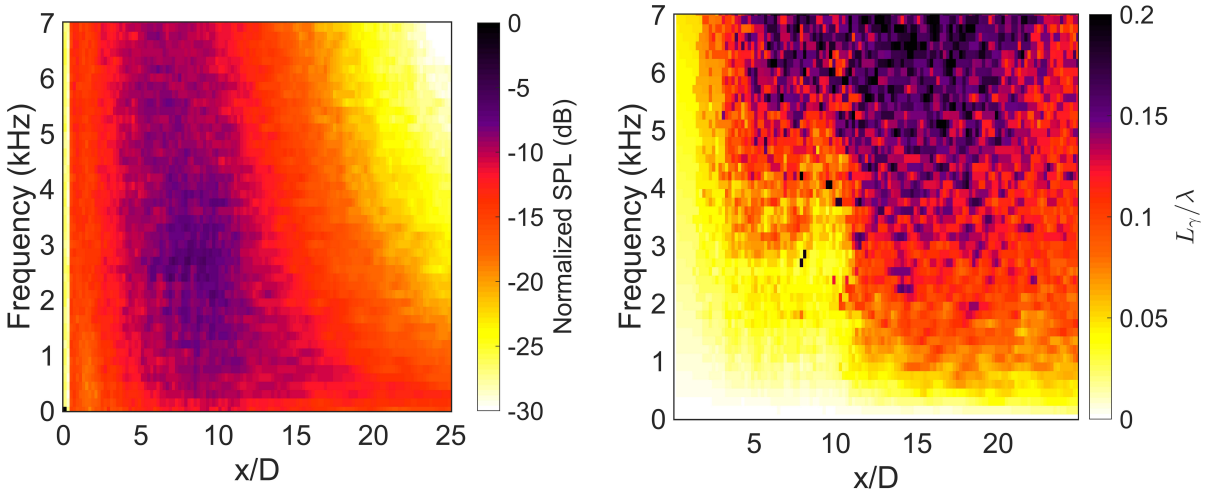

Fig. 4 Level and normalized coherence lengths of the pressures along the nozzle lipline

local acoustic wavelength based on the ratio of specific heats, γ, the temperature, T, of the flow at the reference location, the frequency, f, of interest, and the specific gas constant for air R: $\lambda = c/f = \sqrt{\gamma RT}/f$. The maximum levels along the lipline in Fig. 4 are between 3-15 D downstream of the nozzle. Downstream of 15 D, levels decrease at all frequencies, with the lowest frequencies decaying the slowest. At frequencies below 3.5 kHz and between 3 and 10 D, there are vertical stripes in the level that appear to be due to the influence of the shock cells seen in the fluctuations in Fig. 1.

For this study, the complex pressures along the nozzle lipline were sampled at a 0.2 D intervals. Since L_{γ^2}/λ is small in this region (about $1/20^{\text{th}}$ of the values along the field array), a linear interpolation of the coherence between sampled points was used to avoid discretization errors. Coherence lengths start small at the nozzle exit and quickly increase as the reference is moved downstream, with larger normalized coherence lengths at high frequency. From x/D = 3 D to 10 D, the coherence lengths are shortened at frequencies below 4 kHz. This is in the same region that vertical striations are visible in the level and where shock cells are present.

D. Coherence Between the Flow and the Field

Though coherence does not necessarily imply a cause and effect relationship, coherence between quantities in the flow and in the field show where similar information is included, which can direct further investigation of potential source mechanisms responsible for the far-field acoustics. First, $\mathbf{\Gamma}^2(f)$ is calculated between the sampled nozzle lipline positions and the field array. Each column (or row) of $\mathbf{\Gamma}^2(f)$ then represents the coherence between a single reference on one array to the entirety of the other. To gain an idea of where the information in the field originates in the flow, for each point along the field array, the frequency-averaged coherence was calculated with the pressures along the nozzle

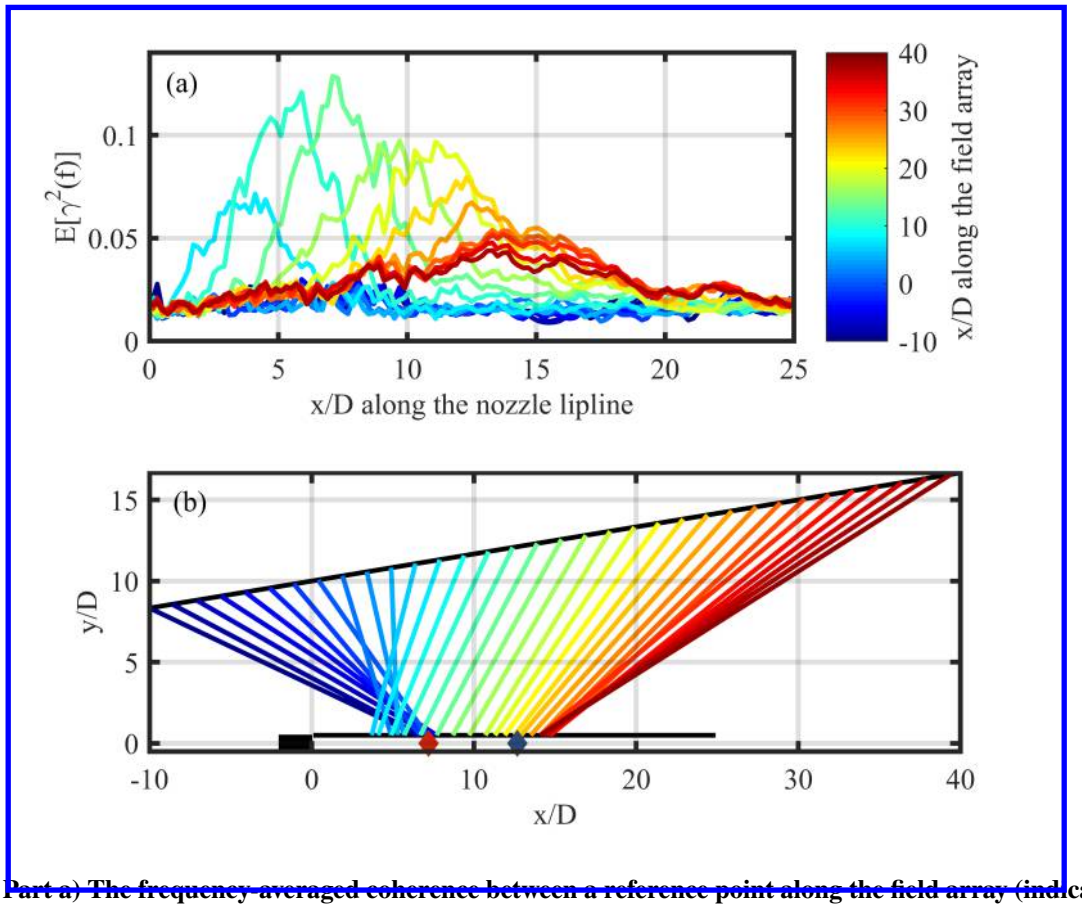

Fig. 5 Part a) The frequency-averaged coherence between a reference point along the field array (indicated by color) and sampled points along the nozzle lipline. Part b) Lines traced between points along the field array and the corresponding point of maximum frequency-averaged coherence along the nozzle lipline.

lipline. Each colored line in Figure 5 a) is the frequency-averaged coherence with respect to a particular reference point along the field array, the position of which is indicated by the color bar. For upstream references in the field (dark blues), the average coherence is low, with small rise above the noise floor between $x/D = 5$ and 10 along the lipline. For references between $x/D = 5$ and 20 on the field array (light blues, teals, greens, and yellows) the coherence peaks, shifts downstream, and decays; all while maintaining a similar width. For references beyond 20 D along the field array, the coherence peak widens, lowers in amplitude, and settles around $x/D = 15$ along the nozzle lip.

To visualize this transfer of information from the flow pressures to the field pressures, Fig. 5 b) shows a schematic of the jet with lines traced from points along the field array to the corresponding points on the nozzle lipline where the frequency-averaged coherence (plotted in part a)) peaks. Because the curves in Fig. 5 a) are quite noisy, they were each smoothed and fit to a sum of two Gaussians, and the peak of the fitted curve was used. It can be immediately seen that different portions of the field are related to specific regions of the flow. The upstream field, which is characterized by the BBSAN, shares coherent information with the flow between $x/D = 6$ and $x/D = 7.5$. The region of maximum radiation, which in Fig. 2 is seen as $10 < x/D < 30$, shares information with the flow region $5 < x/D < 14.5$. The field along the 10 D array beyond the region of maximum radiation (x/D >30, the red lines) all collapse to a region around $x/D = 15$ along the nozzle lipline. Region 2) in the field is characterized by low field coherence, and subsequently has low coherence between the field and the nozzle lipline and does not have a traceable corresponding flow region. Its influence is seen as extra disorder in the traced lines in the transition from region 1) to region 3). A summary of the spatial extent of the corresponding field and flow regions is contained in Table 1.

The cyan, green, and yellow lines in part b) of Fig. 5 all share a similar slope and do not cross, suggesting that the radiation is very directional in that portion of the field. In conjunction with the coherence lengths observed in Figs. 4 and 2, the source could be described as a multiplicity of spatially-ordered, overlapping source regions (not unlike wavepackets) each with some sort of self-coherent phase relationship causing directional radiation (e. g. Mach wave radiation) that propagates to the field. Beyond $x/D = 13$, however, the qualitative nature in the transfer of

Table 1 Summary of the spatial ranges of each field region described in Sec. IV.B as well as the corresponding flow regions based on the analysis in Fig. 5.

	Flow Extent	Field Extent
Region 1)	$6 < x/D < 7.5$	$x/D < 2$
Region 2)	-	$2 < x/D < 5$
Region 3)	$2.7 < x/D < 13$	$5 < x/D < 25$
Region 4)	$13 < x/D < 17$	$25 < x/D$
Region of maximum radiation	$5 < x/D < 15$	$10 < x/D < 30$

information from near to far field changes. The entirety of the field array beyond $x/D = 30$ contains information from an extended region centered around $x/D = 15$ along the lipline. It appears that the nature of the sound radiating from this region of the nozzle lipline switches to be more omnidirectional, instead of the highly directional radiation seen farther upstream. This switch explains why the aft portion of the field array has an increase in coherence as seen in Figs. 2 and 3. Omnidirectional radiation combined with the angle of the field array would result in near grazing incidence of the sound field at the far aft locations.

Based on Fig. 5, there appears to be three important regions in the flow. Upstream where the BBSAN and the aft radiation are originating from same location, the middle where the unidirectional radiation alone is present, and downstream where the information in the far aft acoustic field originates. To look for phenomenological differences in these regions, three references were chosen along the nozzle lipline, and for each reference the coherence spectrum with the field array is calculated. The first two references were chosen as the traced point to the nozzle lipline that corresponds to the point along the field array chosen for parts c) and d) of Fig. 3. The third point is where the farthest aft point on the field array traces back to the nozzle lipline, $x/D = 14.1$. Figure 6 shows the coherence spectrum of the field array with these three reference points along the nozzle lipline, with the 6 dB-down region of the levels as displayed in Fig. 2 for scale.

Figure 6 a) shows the coherence between $x/D = 6.7$ on the nozzle lipline to the entirety of the field array. This position in the flow transmits information to the acoustic field both upstream as BBSAN and downstream to the region of maximum radiation. The transmitted information to the region of maximum radiation seems to segment itself into spatiospectral minima and maxima. This is the first hint of spatiospectral lobe separation in the region of maximum radiation seen in this data set. Part b) shows the coherence with a point farther downstream on the lipline, and it appears to fill out the region of maximum radiation where the field in part a) did not cover. Also, all evidence of coherence with the BBSAN region upstream disappears, even though the frequency content is similar. The reference point for part b) along the lipline is at $x/D = 11.1$, which, as is seen in Fig. 4, is just beyond the influence of the shock cells. Part c) uses a reference at $x/D = 14.1$, and seems to influence the field in a different way than parts a) and b). The coherence consists of low frequencies (predominantly under 2 kHz) and is spread over a larger spatial region in the field. It does overlap with the low frequency portion of part b), which suggests a gradual transition between the source mechanism responsible for the unidirectional radiation in parts a) and b) to this qualitatively different phenomenon in part c).

The red and blue diamonds from Fig. 1 representing the locations of the end of the potential and supersonic cores, respectively, are superimposed on Fig. 5. All of the BBSAN information appears to localize to upstream of the potential core, the far downstream information originates after the end of the supersonic core, and the unidirectional radiation originates all along the jet upstream of the end of the supersonic core. The qualitative difference between the radiation originating upstream of and downstream of the supersonic core is easily described with the wavepacket analogy for jet noise [34]. If the wavepacket is situated upstream of the end of the supersonic core, then the phase relationship of the coherent wavepacket is supersonic, which results in efficient, directional Mach wave radiation. As these turbulent eddies propagate downstream, however, they grow in size and slow down, until after the supersonic core they are no longer supersonic. This causes the phase speed of their wavepacket representation to be subsonic, which results in only a portion of their wavenumber spectrum to radiate efficiently, with the range of supersonic wavenumbers radiating at corresponding ranges of angles, causing less unidirectional radiation.

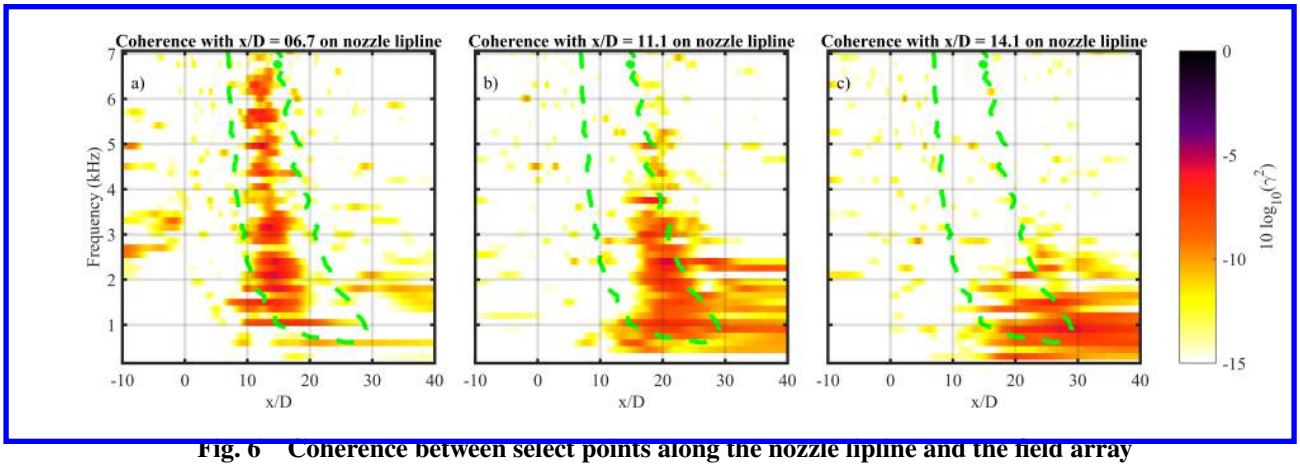

Fig. 6 Coherence between select points along the nozzle lipline and the field array

V. Comparison to the F-35B

High-fidelity measurements of the jet noise produced by military aircraft have been achieved in recent years [14, 35]. Analyses of near-field measurements of the noise from a tied-down F-35B aircraft have shown significant deviation from the traditional two-source model [15, 18], and are phenomenologically compared to the LES of the highly-heated jet here.

The measurement of the F-35B was performed at Edwards Air Force Base in 2013 [35]. The aircraft was tied down to a concrete run-up pad and its engine cycled from 13% engine thrust request (ETR) up through 150% ETR. Engine powers greater than 100% ETR are due to the addition of afterburner. The nozzle of the engine was 2.0 m from the ground and had a nominal 1 m diameter, though the exact nozzle diameter changed with engine condition. The origin of the coordinate system used in this study is at the nozzle exit with the jet plume faced down the positive x-axis. The y-axis is the distance from the jet centerline and the z-axis is the height above the ground. The array was laid out to the left side of the aircraft as shown in Ref. [35], though for convenience all plots here are mirrored to show it on the right side of the aircraft. This study focuses on a 32 m long, 71-element (0.45 m inter-element spacing) linear ground array placed approximately parallel to the shear layer, which is shown in Fig. 7. The recorded 30-second time waveforms (204.8 kHz sampling frequency) were split into multiple blocks with a 50% overlap, windowed with a Hann function, then the Fourier transform was applied to each block. Swift *et al*. [18] analyzed the full, high-resolution data set. For this work, to be able to compare more closely with the LES of the heated laboratory-scale jet, the block size was adjusted to give a frequency resolution of 15 Hz and only 97 blocks were used.

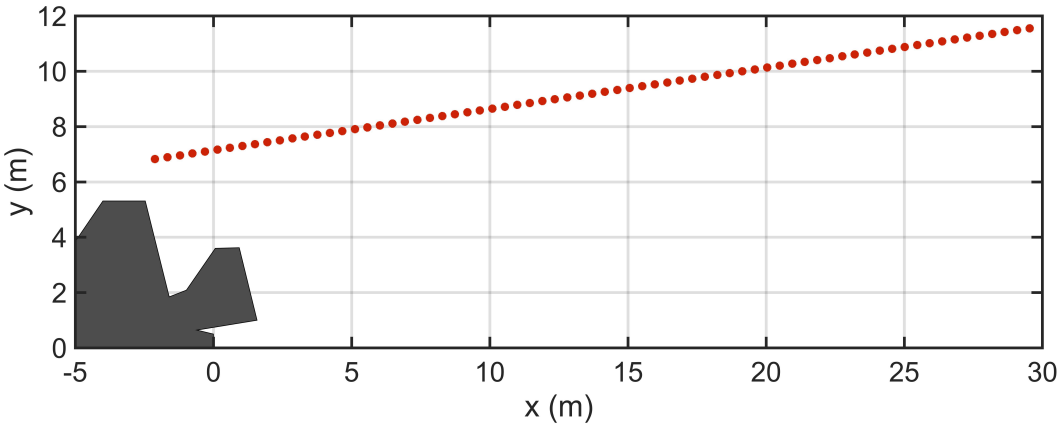

Fig. 7 Schematic of the linear ground array used to measure the jet noise field of the F-35B.

The temperature ratio in the LES analyzed in this study was chosen to be similar to a tactical aircraft operating at

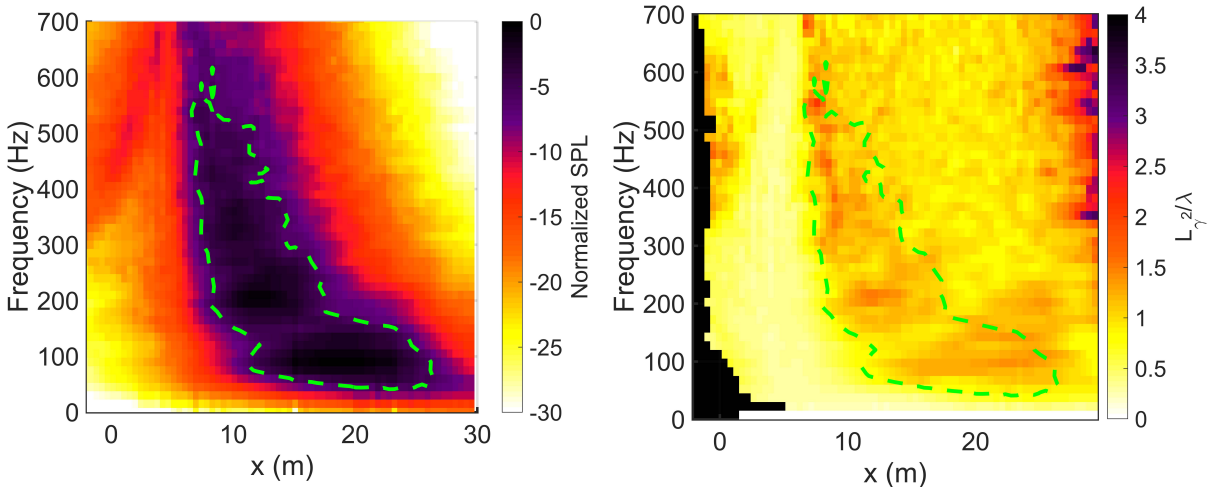

Fig. 8 Spatiospecral map and normalized upstream coherence lengths from F-35B aircraft operating at 150% ETR. Left: measured spectra along the linear ground array approximately parallel to the shear layer. Right: upstream coherence length calculated along the same array.

afterburner, so the 150% ETR case of the F-35B measurement is studied here. The only attempt to scale either data set for comparison was the normalization of levels and choice of frequency range and resolution. The normalized spectrum measured along the array is displayed in the left pane of Fig. 8. BBSAN is seen upstream starting at 350 Hz, increasing to almost 700 Hz at $x = 5$ m. The directional portion of the turbulent mixing noise dominates from 5-30 m downstream, with as many as 6 spatiospectral lobes present. The lowest, farthest aft lobe appears to split into two, with one lobe having a distinct spatiospectral slope similar to the other high-frequency lobes and the other having a horizontal slope.

The calculated upstream coherence lengths for the F-35B measurement were first shown in Ref. [18] and are repeated here in Fig. 8 (though this study uses a coarser frequency resolution for comparison to the LES). There is a similar trend as the LES with the coherence lengths being large upstream due to the presence of BBSAN, small in the region dominated by sideline radiation, increasing again in the region of maximum radiation, further increasing at low frequencies farther downstream, then saturating at high frequencies at the end of the array where the it appears to be measuring a progressive wave field. The most apparent feature of Fig. 8 is an oscillation of high and low coherence length value in the region of maximum radiation that correspond to the multiple spatiospectral lobes. These spatiospectral lobes were investigated more in depth by Refs. [15, 18, 22], and the drop in coherence length is believed to be due to the mixing of the field from the multiple incoherent spatiospectral lobes.

The pattern of Fig. 8 is qualitatively similar to the pattern seen in Fig. 2, except the LES does not contain the distinct lobing that is obvious in the F-35 data. It is unknown at this point why the LES does not contain this phenomenon. When looking at the color maps for both the LES and the F-35, the background coherence lengths seem to remain yellow and orange, with the red regions superimposed on top. In the F-35 case, the red regions group to produce the spatiospectral lobe phenomenon, but in the case of the LES the red is sprinkled throughout the maximum radiation region.

To investigate source regions of the flow responsible for crackle in the F-35 aircraft, Vaughn *et al*. [36] use an event-based beamforming technique to localize the sources of events with high derivatives. They found that all along the same array discussed in this paper, the high derivative events localize to locations upstream of $x = 12$ m. Additionally, Leete *et al*. [15] used an advanced acoustical holography technique to reconstruct the acoustic field of the F-35 from this same data set and found that though the majority of the time-averaged energy comes from upstream of $x = 20$ m, when individual lobes are traced back to the jet centerline, the lowest frequency and farthest downstream lobe traces to locations beyond $x = 10$ m, while the higher frequency lobes all trace to locations upstream of $x = 10$ m. The tracing of the coherent energy in the LES shown in Fig. 5 in this work shows a similar pattern, with the low frequency, downstream information (red lines of Fig. 5) tracing back to locations further downstream than the regions dominated by higher frequency content (cyan, green, and yellow lines of Fig. 5). The connection between spatiospectral lobes, source regions in the flow, and field characteristics of full-scale aircraft is an ongoing research problem.

VI. Conclusions

Level and coherence analyses of the simulated noise from a highly-heated jet leads to the identification of at least four distinct field regions. Region 1) is characterized by the presence of BBSAN, where the characteristic spatially-dependant self-coherent spectra appears upstream with a corresponding source region shared with some of the downstream radiation (region 3)). Region 2) is the region of low coherence towards the sideline of the jet, upstream of the region of maximum radiation. Region 3) is the upstream portion of the region of maximum radiation. It is partially self-coherent and partially coherent with the BBSAN upstream. It originates from overlapping segments of spatially-ordered self-coherent regions of the flow pressures with highly directional radiation. Region 4) begins with the low-frequency portion of the region of maximum radiation and extends downstream. A broad, partially coherent region in the flow pressures transmits information to a large area in the field, implying less directional radiation. Similar to previous studies of high-performance military aircraft, [15, 18] regions 1), 3) and 4) could be thought of as spatiospectral lobes, which coincides with previous studies of this LES data set [26] that discusses the dual peaks found in the spectrum at certain field locations.

Identification of separate source regions in the flow with differing coherence properties suggest that the source mechanisms involved in producing the various field regions are fundamentally different. Traditionally, the directional radiation in the aft direction has been attributed solely to the Mach wave radiation of large-scale turbulent structures. It is seen with this LES that the large-scale turbulent structure noise originating from the supersonic portion of the flow transmits its energy more efficiently to the field in the characteristic unidirectional pattern associated with Mach wave radiation. Downstream of the end of the supersonic core, the transfer of information from flow to field is less efficient and unidirectional, characteristic of only portions of the wavenumber spectrum of the coherent wavepacket radiating efficiently. This then explains the two spatiospectral lobes as seen in the LES. The lowest frequency spatiospectral lobes present in the F-35 could be similarly explained with this same line of reasoning if the Mach number of the flow was known. However, other than slight evidence of high-frequency spatiospectral lobe formation in the flow to field coherence spectra shown here, there is no explanation of the presence of so many spatiospectral lobes in the F-35.

At this point, bringing LES of a laboratory-scale jet to high temperatures (designed to be in the same regime as high-performance military aircraft operating at afterburner) does not account for all of the spatiopspectral lobe content that is observed in the F-35B [15], but the four regions identified in this paper do seem to apply generally. Splitting of the field into spatiospectral lobes is only seen in this data set in the coherence between the flow and the field in a region where shock cells are present in the flow, suggesting that shock cells may play a role. Additional laboratory-scale tests or LES operating at even more realistic high-performance military aircraft conditions are needed to fully understand the spatiospectral characteristics of the F-35B.

VII. Acknowledgments

This research was supported in part by the Office of Naval Research through the Jet Noise Reduction Project. The authors also gratefully acknowledge funding for the F-35 measurements provided through the F-35 Program Office and Air Force Research Laboratory. K. M. Leete was funded by an appointment to the Student Research Participation Program at the U.S. Air Force Research Laboratory, 711$^{\text{th}}$ Human Performance Wing, Human Effectiveness Directorate, Warfighter Interface Division, Battlespace Acoustics Branch administered by the Oak Ridge Institute for Science and Education through an interagency agreement between the U.S. Department of Energy and USAFRL. (Distribution A: Approved for public release; distribution unlimited. Cleared 03/25/2019 JSF19-225).

References

[1] Laufer, J., Schlinker, R. H., and Kaplan, R. E., "Experiments on supersonic jet noise," *AIAA Journal*, Vol. 14, 1976, pp. 489–497.

[2] Tam, C., Golebiowski, M., and Seiner, J., *On the two components of turbulent mixing noise from supersonic jets*, Aeroacoustics Conferences, American Institute of Aeronautics and Astronautics, 1996. doi:10.2514/6.1996-1716.

[3] Lee, H. K., and Ribner, H. S., "Direct Correlation of Noise and Flow of a Jet," *The Journal of the Acoustical Society of America*, Vol. 52, 1972, pp. 1280–1290.

[4] Crow, S. C., and Champagne, F. H., "Orderly structures in jet turbulence," *Journal of Fluid Mechanics*, Vol. 48, 1971, pp. 547–591.

[5] Brown, G. L., and Roshko, A., "On density effects and large structures in turbulent mixing layers," *Journal of Fluid Mechanics*, Vol. 64, 1974, pp. 775–816.

[6] Bogey, C., and Bailey, C., "An analysis of the correlations between the turbulent flow and the sound pressure fields of subsonic jets," *Journal of Fluid Mechanics*, Vol. 583, 2007, pp. 71–97.

[7] Panda, J., and Seasholtz, R. G., "Experimental investigation of density fluctuation in high-speed jets and correlation with generated noise," *Journal of Fluid Mechanics*, Vol. 450, 2002, pp. 97–130.

[8] Panda, J., Seasholtz, R. G., and Elam, K. A., "Investigation of noise sources in high-speed jets via correlation measurements," *Journal of Fluid Mechanics*, Vol. 537, 2005, pp. 349–385.

[9] Tam, C. K. W., and Auriault, L., "Jet mixing noise from fine-scale turbulence," *AIAA Journal*, Vol. 37, 1999, pp. 145–153.

[10] Tam, C. K. W., Viswanathan, K., Ahuja, K. K., and Panda, J., "The sources of jet noise: experimental evidence," *Journal of Fluid Mechanics*, Vol. 615, 2008, pp. 253–292.

[11] Tam, C. K. W., and Chen, K. C., "A statistical model of turbulence in two-dimensional mixing layers," *Journal of Fluid Mechanics*, Vol. 92, 1979, pp. 303–326.

[12] Neilsen, T. B., Gee, K. L., Wall, A. T., and James, M. M., "Similarity spectra analysis of high-performance jet aircraft noise," *The Journal of the Acoustical Society of America*, Vol. 133, 2013. doi:10.1121/1.4792360.

[13] Neilsen, T. B., Vaughn, A. B., Gee, K. L., Swift, S. H., Wall, A. T., Downing, J. M., and James, M. M., *Inclusion of Broadband Shock-Associated Noise in Spectral Decomposition of Noise from High-performance Military Aircraft*, AIAA AVIATION Forum, American Institute of Aeronautics and Astronautics, 2018. doi:10.2514/6.2018-3146.

[14] Wall, A. T., Gee, K. L., James, M. M., Bradley, K. A., McInerny, S. A., and Neilsen, T. B., "Near-field noise measurements of a high performance military jet aircraft," *Noise Control Engineering Journal*, Vol. 60, 2012, pp. 421–434.

[15] Leete, K. M., Wall, A. T., Gee, K. L., Neilsen, T. B., James, M. M., and Downing, J. M., *Dependence of High-performance Military Aircraft Noise on Frequency and Engine Power*, AIAA AVIATION Forum, American Institute of Aeronautics and Astronautics, 2018. doi:10.2514/6.2018-2826.

[16] Stout, T. A., Gee, K. L., Neilsen, T. B., Wall, A. T., and James, M. M., "Acoustic intensity near a high-powered military jet aircraft," *The Journal of the Acoustical Society of America*, Vol. 138, 2015, p. EL1.

[17] Stout, T. A., Gee, K. L., Neilsen, T. B., Wall, A. T., and James, M. M., "Source characterization of full-scale jet noise using acoustic intensity," *Noise Control Engr. J.*, Vol. 63, No. 6, 2015, pp. 522 – 536.

[18] Swift, S. H., Gee, K. L., Neilsen, T. B., Wall, A. T., Downing, J. M., and James, M. M., *Spatiotemporal-correlation analysis of jet noise from a round nozzle high-performance aircraft*, AIAA AVIATION Forum, American Institute of Aeronautics and Astronautics, 2018. doi:10.2514/6.2018-3938.

[19] Wall, A. T., Gee, K. L., and Neilsen, T. B., "Multisource statistically optimized near-field acoustical holography," *The Journal of the Acoustical Society of America*, Vol. 137, 2015, pp. 963–975.

[20] Wall, A. T., Gee, K. L., Neilsen, T. B., McKinley, R. L., and James, M. M., "Military jet noise source imaging using multisource statistically optimized near-field acoustical holography," *The Journal of the Acoustical Society of America*, Vol. 139, 2016, pp. 1938–1950.

[21] Wall, A. T., Leete, K. M., Gee, K. L., Neilsen, T. B., James, M. M., and McKinley, R. L., *Preliminary Investigation of Multilobe Fighter Jet Noise Sources Using Acoustical Holography*, AIAA AVIATION Forum, American Institute of Aeronautics and Astronautics, 2017. doi:10.2514/6.2017-3520.

[22] Wall, A. T., Gee, K. L., Leete, K. M., Neilsen, T. B., Stout, T. A., and James, M. M., "Partial-field decomposition analysis of full-scale supersonic jet noise using optimized-location virtual references," *The Journal of the Acoustical Society of America*, Vol. 144, No. 3, 2018, pp. 1356–1367. doi:10.1121/1.5053580.

[23] Tam, C. K., Aubert, A. C., Spyropoulos, J. T., and Powers, R. W., *On the Dominant Noise Components of Tactical Aircraft: Laboratory to Full Scale*, AIAA AVIATION Forum, American Institute of Aeronautics and Astronautics, 2017. doi:10.2514/6.2017-3516.

[24] Long, D., *Jet Noise Source Location via Acoustic Holography and Shadowgraph Imagery*, Aeroacoustics Conferences, American Institute of Aeronautics and Astronautics, 2008. doi:10.2514/6.2008-2888.

[25] Liu, J., Corrigan, A. T., Kailasanath, K., and Gutmark, E. J., *Impact of Chevrons on Noise Source Characteristics In Imperfectly Expanded Jet Flows*, AIAA AVIATION Forum, American Institute of Aeronautics and Astronautics, 2015. doi:10.2514/6.2015-2835.

[26] Liu, J., Corrigan, A. T., Kailasanath, K., and Taylor, B. D., *Impact of the Specific Heat Ratio On the Noise Generation in a High-Temperature Supersonic Jet*, AIAA SciTech Forum, American Institute of Aeronautics and Astronautics, 2016. doi:10.2514/6.2016-2125.

[27] Liu, J., Kailasanath, K., and Gutmark, E. J., *Similarity Spectra Analysis in Highly Heated Supersonic Jets Using Large-Eddy Simulations*, AIAA SciTech Forum, American Institute of Aeronautics and Astronautics, 2017. doi:10.2514/6.2017-0926.

[28] Harker, B. M., Neilsen, T. B., Gee, K. L., Wall, A. T., and James, M. M., "Spatiotemporal-Correlation Analysis of Jet Noise from a High-Performance Military Aircraft," *AIAA Journal*, Vol. 54, No. 5, 2016, pp. 1554–1566.

[29] Leete, K. M., Gee, K. L., Neilsen, T. B., Harker, B. M., Wall, A. T., and James, M. M., "Azimuthal coherence of the sound field in the vicinity of a high-performance military aircraft," *Proc. Mtgs. Acoust.*, Vol. 29, 2016, p. 045007. doi:10.1121/2.0000673.

[30] Walton, J. T., and Burcham, F. W., "Exhaust-gas pressure and temperature survey of F404-GE-400 turbofan engine," *NASA Technical Memorandum*, Vol. 88273, 1986. URL `https://ntrs.nasa.gov/archive/nasa/casi.ntrs.nasa.gov/19880010923.pdf`.

[31] Bendat, J. S., and Piersol, A. G., *Random Data*, 2nd ed., 1986.

[32] Liu, J., Corrigan, A. T., Kailasanath, K., Heeb, N. S., and Gutmark, E. J., *Numerical Study of Noise Sources Characteristics in An Underexpanded Jet Flow*, AIAA AVIATION Forum, American Institute of Aeronautics and Astronautics, 2014. doi:10.2514/6.2014-2604.

[33] Wall, A. T., Gardner, M. D., Gee, K. L., and Neilsen, T. B., "Coherence length as a figure of merit in multirefrence near-field acoustical holography," *The Journal of the Acoustical Society of America*, Vol. 132, 2012, p. EL215. doi:10.1121/1.4740518.

[34] Jordan, P., and Colonius, T., "Wave Packets and Turbulent Jet Noise," *Annual Review of Fluid Mechanics*, Vol. 45, No. 1, 2013, pp. 173–195. URL `https://doi.org/10.1146/annurev-fluid-011212-140756`.

[35] James, M. M., Salton, A. R., Downing, J. M., Gee, K. L., Neilsen, T. B., Reichman, B. O., McKinley, R., Wall, A. T., and Gallagher, H., *Acoustic Emissions from F-35 Aircraft during Ground Run-Up*, AIAA AVIATION Forum, American Institute of Aeronautics and Astronautics, 2015. doi:10.2514/6.2015-2375.

[36] Vaughn, A. B., Gee, K. L., Swift, S. H., Wall, A. T., Downing, J. M., and James, M. M., "Beamforming of supersonic jet noise for crackle-related events," *Proc. Mtgs. Acoust.*, Vol. 35, 2018, p. 040003. doi:10.1121/2.0000998.